J Nanopart Res (2013) 15:1440
DOI 10.1007/s11051-013-1440-9

RESEARCH PAPER

Effect of monobutylether ethylene glycol on Mg/Al layered double hydroxide: a physicochemical and conductivity study

Maria Joao Paulo · Bruno Ribeiro de Matos · Spyridon Ntais · Fabio Coral Fonseca · Ana C. Tavares

Received: 3 July 2012 / Accepted: 12 January 2013

Abstract Mg–Al hydrotalcite-like compounds with OH^- ions intercalated in the gallery and modified with monobutylether ethylene glycol (*mbeeg*) were prepared from $Mg_6Al_2(CO_3)(OH)_{16}{\cdot}4H_2O$ by the reconstruction method. The effect of the ethylene glycol, a moderate surfactant, on the textural properties and on the vapor water sorption of the layered double hydroxides was investigated by transmission electron microscopy and nitrogen and water sorption techniques. The ion conductivity of the samples was measured at 98 % RH up to 180 °C. The compounds are formed by nanoplatelets with a lateral size inferior to 20 nm. The addition of the ethylene glycol was found to increase the specific surface area, total pore volume, and water sorption capacity of the Mg–Al layered double hydroxide. However, it also decreased the average pore diameter, and the ion conductivity of the ethylene glycol modified layered double hydroxide was lower than expected based on the samples' specific surface area and water content.

M. J. Paulo · S. Ntais · A. C. Tavares (✉)
Institut National de la Rechercher Scientifique – Énergie, Matériaux et Télécommunications, 1650 Boulevard Lionel-Boulet, Varennes, QC J3X 1S2, Canada
e-mail: tavares@emt.inrs.ca; ana.tavares@emt.inrs.ca

B. R. de Matos · F. C. Fonseca
Instituto de Pesquisas Energéticas e Nucleares – IPEN-CNEN/SP, Avenida Lineu Prestes, 2242, São Paulo, SP 05508000, Brazil

Keywords Layered double hydroxide · Hydrotalcite · Monobutylether ethylene glycol · Textural properties · Water sorption · Ion conductivity

Introduction

Since the issue of the first patent on the use of a hydrotalcite-like compound as a precursor for the preparation of hydrogenation catalysts (Bröcker and Kainer 1970), these materials have attracted the scientific interest. Hydrotalcite-like compounds, also referred as layered double hydroxides (LDHs), can be described by the general formula $\left[\left[M(II)_{1-x}M(III)_x(OH^-)_2\right]\right]^{x+}(A^{n-})_{x/n}\cdot mH_2O$ (where M(II) and M(III) are divalent and trivalent cations, respectively, and A^{n-} is an anion. Their structure is based on brucite-like two-dimensional layers, and the anions are intercalated between the positively charged hydroxide layers.

The most representative compound of the LDH family is hydrotalcite where Mg^{2+} and Al^{3+} stand for M(II) and M(III) and CO_3^{2-} is the anion in the gallery. A wide variety of LDHs-containing various divalent and trivalent cations [M(II): Mg, Zn, Ni, and Cu; M(III): Al, Ga, In, Cr, and Fe] in combination with different anions [NO_3^-, Cl^-, ClO_4^-, SO_4^{2-}, CrO_4^{2-}, CO_3^{2-}] have been reported (Miyata 1975; Miyata and Okada 1977; Reichle 1986; Cavani et al. 1991; Aramendia et al. 1999; Feng et al. 2003).

Published online: 24 January 2013

LDHs have found widespread application in areas like catalysis (Gusmano et al. 1991; Traversa et al. 1992a, b; Tichit et al. 1995; Béres et al. 1999), in biochemistry (Trikeriotis and Ghanotakis 2007), and as adsorbents (Hussein and Hwa 2000). More recently, due to their ion conduction properties, LDHs started to be considered as attractive electrolyte materials in power generation systems such as Li batteries (Liao and Ye 2003; Liao and Ye 2003; Cho et al. 2004; Borgohain et al. 2010; Li et al. 2006) and fuel cells (Lee et al. 2005; Lee and Nam 2006; Miyazaki et al. 2010; Kim et al. 2010; Tadanaga et al. 2010; Furukawa et al. 2011). Particularly promising is the use of LDHs as solid electrolytes in alkaline direct alcohol fuel cells (Tadanaga et al. 2010; Furukawa et al. 2011; Kim et al. 2010; Paulo and Tavares 2011) since the success of this type of fuel cells depends on the development of anion exchange membranes resistant to the strong oxidative and alkaline environment (Varcoe and Slade 2005; Hickner 2010). Indeed, the use of these compounds in alkaline fuel cells is motivated by their stability at high pH. Recently, a 0.4-cm^2 pelletized hydrotalcite sample was tested as electrolyte in direct ethanol fuel cell (DEFC) and a maximum power density of 65 mW cm^{-2} was obtained at 80 °C (Tadanaga et al. 2010).

Early studies (Lal and Howe 1980, 1981; De Roy et al. 1985; Moneyron et al. 1991) demonstrated that LDHs exhibit both anionic and protonic conductivity. According to these studies, the conductivity is influenced by the composition of the LDH, the temperature, and the relative humidity (Pernice et al. 1988; De Roy and Besse 1989). The mobility of the anions is strongly affected by the water content in the gallery (Allmann 1968, 1970; De Roy and Besse 1989). On the other hand, (Yun and Pinnavaia 1995) showed that different synthetic routes have a significant impact on the textural properties of Al–Mg–CO_3^{2-} LDHs and on the amount of three types of adsorbed water, namely inter-particle water, extrinsic, and intrinsic surface bound water. Still, few studies address the effect of the textural properties on the ion conductivity of hydrotalcite-like compounds. The recent studies targeted to alkaline fuel cells focused on the evaluation of the ion conductivity of Mg–Al hydrotalcite-like compounds intercalated with different anions (CO_3^{2-}, Cl^-, Br^-, SO_4^{2-}, and OH^-) (Furukawa et al. 2011), as a function of the Mg/Al ratio on Mg–Al–CO_3^{2-} and Mg–Al–OH^- LDHs (Kim et al. 2010) and as a function of the particle size on Mg–Al–CO_3^{2-} (Tamaki et al. 2012).

The present work focus on meixnerite, the Mg–Al hydrotalcite-like compound with OH^- ions intercalated in the gallery, and on its modification with monobutylether ethylene glycol (*mbeeg*). *Mbeeg* is a moderate surfactant and was used to induce textural modifications on the Mg–Al double layered hydroxide, through the interaction of its hydrophilic part, the glycol ether function, with the hydroxide layers. *Mbeeg* was chosen because of its miscibility with water since in this work the LDHs were synthesized from hydrotalcite by the reconstruction method (Miyata 1983).

The materials were characterized in terms of their composition, structure, textural properties, water vapor sorption, and ion conductivity between 20 and 180 °C at 98 % RH. The objective of this work is to obtain a better insight on the relationship between the textural and the conduction properties of the hydrotalcite-like compounds with similar composition.

Experimental

Materials

Hydrotalcite powder ($Mg_6Al_2(CO_3)(OH)_{16}{\cdot}4H_2O$) referred hereafter as HT–CO_3^{2-} was purchased from Sigma-Aldrich Co. *Mbeeg* 97 % was purchased from Fisher Scientific. Decarbonated water was used for the preparation of the modified LDHs.

Methods

Meixnerite ($Mg_6Al_2(OH)_{18}{\cdot}4H_2O$) was synthesized through the reconstruction method (Miyata 1983). Initially, HT–CO_3^{2-} was calcined at 500 °C for 3 h to form a magnesium–aluminum mixed oxide. After cooling to room temperature, the mixed oxide was dispersed in degassed water and stirred vigorously for 16 or 21 h under N_2 flow. The final compounds, named as HT–OH^--16 h and HT–OH^--21 h, were filtered, dried under vacuum for 2 h, and stored in a desiccator.

Meixnerite modified with *mbeeg* (referred hereafter as HT–OH^-–*mbeeg*) was synthesized from HT–OH^--16 h. After hydration, *mbeeg* was added to the slurry (2:1 vv %) and the obtained solution was stirred under

N_2 flow for additional 5 h, which means that in total the hydration steps lasted 21 h. The final product was filtered, washed with decarbonated water, dried under vacuum for 2 h, and stored in a desiccator.

Characterization

Fourier transformed infrared (FT-IR) spectra were recorded on a NEXUS 670 FT-IR apparatus, in the range of 600–4,000 cm^{-1} range. The powdered samples were mixed with KBr and pressed in the form of pellets for the FT-IR measurements. The spectra were collected using a 4 cm^{-1} resolution and 128 scans.

The samples' carbon content was determined by dynamic flash combustion method using a CHNS/O analyzer-EAS1108 (Fisons instruments, Elemental Analysis Laboratory services of the Université de Montréal).

Powder X-ray diffraction (XRD) patterns were recorded using a Bruker D-8 ADVANCE diffractometer equipped with a LynxEye position sensitive detector, and using a CuKα X-ray source (40 kV, 40 mA). Data were collected over the 2θ range from 3° to 90° in a step mode of 0.02° and 2 s duration (0.01 °/s).

Transmission electron micrographs (TEM) were obtained using a JEOL 2100F operated at 200 kV (Center for Characterization of Microscopic Materials, at Ecole Polytechnique de Montréal). The TEM samples were prepared by dipping copper grids into dispersions of the powders in methanol.

The textural properties of the powders were determined by nitrogen physisorption experiments carried out at −196 °C using a Quantachrome Autosorb-1 Series Surface Area and Pore Size Analyzer. Before the measurements, the samples were outgassed at 100 °C for 2 h under vacuum. The specific surface area was determined from the low pressure region ($P/P_0 < 0.25$) following the BET (Brunauer–Emmett–Teller) procedure and the total pore volume was calculated from the point at $P/P_0 = 0.989$.

Water sorption isotherms were recorded using a Dynamic Vapor Sorption-High Throughput (DVS-HT) apparatus (surface measurement systems) equipped with a Cahn ultra microbalance with a mass resolution of 10 μg. Typically, 10 mg of sample was placed in the DVS-HT pans and dried under a stream of dry N_2 at 25 °C for 6 h to insure that all samples have reached a constant mass before the sorption measurements. Sorption isotherms were recorded at 25 °C as a function of the relative humidity (%RH) with a step time of 3 h from 0 to 90 % RH, followed by a plateau at 97 % for 12 h. Relative humidity was then reduced to 0 % and following the same profile, completing the cycle.

The LHDs ion conductivity was evaluated by two-probe (through-plane) impedance spectroscopy (IS) between 20 and 180 °C and at 98 % RH. Pellets were prepared by pressing the powders with a stainless steel press die at 5 tons for 1 min, sandwiched between two carbon cloth electrodes (to facilitate the equilibrium with water vapors), and finally placed in a homemade Teflon sample holder equipped with stainless steel terminal leads. The sample holder was inserted in an airtight stainless steel chamber containing distilled water. In order to achieve equilibrium between the sample and the measuring RH, the studied samples were kept at room temperature and 98 %RH for 24 h before conductivity measurements (Alberti et al. 2001). A frequency response analyzer (Solartron 1260) was used and the amplitude of the sinusoidal wave was 100 mV in the 1 Hz–3 MHz frequency interval. The total electrical resistance (dc) was obtained at the intercept of the low frequency portion of the diagram with the real axis in Nyquist plots. The conductivity values were calculated by the following equation: $\sigma = (1/R)\,(l/S)$, where σ is the conductivity (S cm^{-1}), R is the resistance (ohm), l is the sample thickness (cm), and S is the contact surface with the electrodes (cm^2).

Results and discussion

FTIR and CHNS analysis

FTIR, CHNS analysis, and XRD measurements were performed to confirm that HT–OH^-–*mbeeg* has the hydrotalcite structure, to verify the nature of the anions in the gallery (CO_3^{2-} vs OH^-) and the presence of *mbeeg* in the modified LDH.

The FTIR spectra are presented in Fig. 1. The absorption peak around 866 cm^{-1} is characteristic of the M–O (M = Al^{3+}, Mg^{2+}) lattice stretching and deformation vibrations and its presence in all samples confirms that the LDH structure is not affected by *mbeeg*. The strong intense vibration at 1,371 cm^{-1} is a characteristic of the CO_3^{2-} groups in the LDH gallery

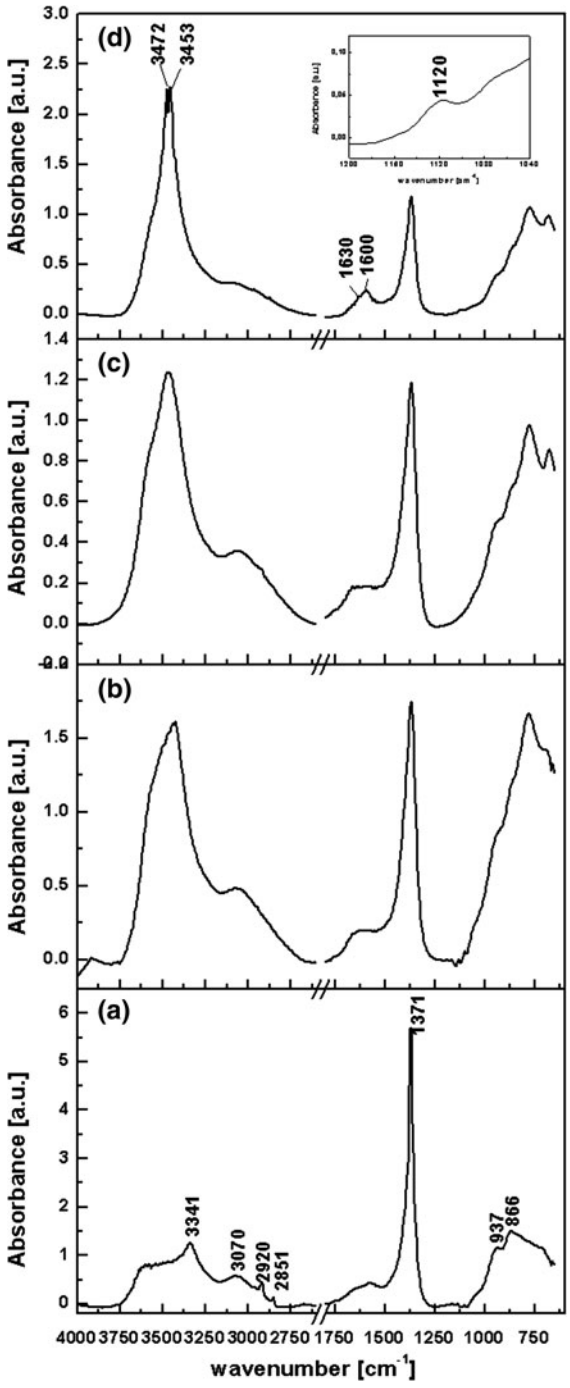

Fig. 1 FT-IR spectra of HT–CO_3^{2-} (**a**), HT–OH^--16 h (**b**), HT–OH^--21 h (**c**), and HT–OH^-–*mbeeg* (**d**) samples

and its intensity is remarkably lower in HT–OH^- and HT–OH^-–*mbeeg* samples with respect to the hydrotalcite precursor. This observation is consistent with a LDH-gallery poorer in CO_3^{2-} anions because of their substitution by OH^- anions. The decrease is more pronounced as the hydration time increases, and is even more marked in the case of the HT–OH^-–*mbeeg*. The conversion of CO_3^{2-} to OH^- is apparently not complete, but as well documented in the literature the re-carbonation of the gallery occurs on exposition of the samples to atmospheric CO_2 (Reeves 2001). The broad absorption band in the region between 2,850 and 3,650 cm^{-1} is related to the stretching vibrations of the OH^- groups of the interstitial water and the hydroxyl groups (Olfs et al. 2009).

In the case of HT–OH^-–*mbeeg*, a new peak around 1,600 cm^{-1} and another one of lower intensity at 1,630 cm^{-1} are detected. According to studies on similar systems, peaks in this area were attributed to the water present in the gallery of LDHs. Yang et al. (2002) reported the decrease of the intensity of the inter-layer water peak around 1,620 cm^{-1} with increasing temperature for Mg–Al–CO_3^{2-} LDHs. Moreover, in the case of organo-functionalized LDHs a similar peak at 1,645 cm^{-1} is attributed to inter-layer H_2O molecules (Muksing et al. 2011). As it is known, glycol ethers have high affinity to water and they retain water molecules through hydrogen bonds (Philippova et al. 1985; Crupi et al. 1995, 1996). Indeed, in studies concerning mixtures of polyethylene glycols (PEGs) with water, a peak around 1,650 cm^{-1} has been attributed to water molecules attached through hydrogen atoms to PEG (Rozenberg et al. 1998). The enhanced intensity of the peaks in this region compared to the HT–OH^--16 h and HT–OH^--21 h strongly suggests that modification with *mbeeg* causes an increase of the inter-layer water content. HT–OH^-–*mbeeg* shows, in addition, two well resolved peaks at 3,453 and 3,472 cm^{-1} that can be attributed to OH stretching modes similarly to the work of Stygar et al. (2005) on alkali metal perchlorate–poly(ethylene glycol) monomethyl ether solutions.

It should be noted at this point that the intensity of the vibration around 1,120 cm^{-1} that is characteristic of C–O–C group (Rozenberg et al. 1998) is very weak. Though this result is consistent with previous studies concerning, the adsorption of ethylene glycol monoethyl ether on montmorillonite (Nguyen et al. 1987). The characteristic C–H stretching vibration mode around 2,930 cm^{-1} (Nguyen et al. 1987) and of the C–C rocking vibrations in the region 900–950 cm^{-1} exhibit very low intensity probably due to the very low content of *mbeeg* in the sample and/or their superposition with

Table 1 Carbon content as determined by elemental analysis

Sample	wt% C
HT–CO_3^{2-}	5.4
HT–OH^--16 h	1.4
HT–OH^--21 h	1.2
HT–OH^-–*mbeeg*	4.4

characteristic peaks of hydrotalcite. Thus, the samples were further analyzed by the elemental analysis so as to attain a better insight concerning the content of *mbeeg*. Table 1 reports the carbon content in all samples as it was determined by CHNS analysis. The carbon wt% decreases from HT–CO_3^{2-} to HT–OH^-, as expected, and with the hydration time. On the other hand, after the modification with *mbeeg*, an almost threefold increase of carbon content compared to HT–OH^--21 h is observed. This result, in combination with the FT-IR results, strongly suggests that *mbeeg* is present on the LDH.

X-ray diffraction

The recorded XRD patterns of the commercial and modified materials are presented in Fig. 2. X-ray diffraction analysis confirmed that HT–OH^-–*mbeeg* has a hydrotalcite-like structure. The basal (*00l*) reflections characteristic of the LDH structure are clearly present, showing that the layered structure is not affected by *mbeeg*. The only change is on the width of the diffraction lines which are broader compared to those of HT–OH^-. No broadening was noticed with the hydration time for the HT–OH^--16 h and HT–OH^--21 h samples. Thus, the peak broadening could result either from a partial loss of crystallinity or from a decrease of the particle size induced by *mbeeg*. Moreover, the (003) crystallographic plane shifts toward lower (2θ) values. Table 2 reports the basal distance $d_{(003)}$ and the unit cell parameters a and c calculated by the following relationships (Yun and Pinnavaia 1995):

$$a = b = 2d_{(110)} \quad (1)$$

and

$$c = 3d_{(003)} \quad (2)$$

The lattice parameters along a and b axis are in the range expected for hydrotalcite and meixnerite

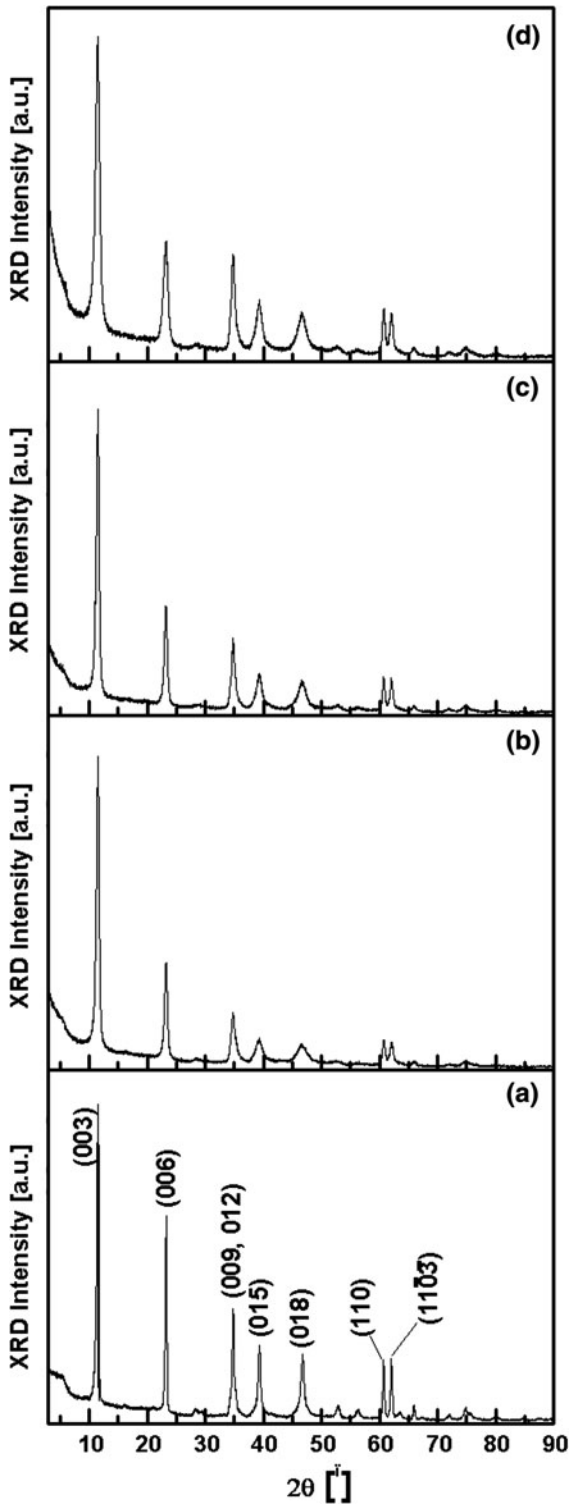

Fig. 2 X-ray diffraction patterns of HT–CO_3^{2-} (**a**), HT–OH^--16 h (**b**), HT–OH^--21 h (**c**), and HT–OH^-–*mbeeg* (**d**) samples

Table 2 Lattice constants a and c and basal distance $d_{(003)}$ for all four samples

Parameter (Å)	HT–CO_3^{2-}	HT–OH^--16 h	HT–OH^--21 h	HT–OH^-–*mbeeg*
$d_{(003)}$	7.662	7.688	7.695	7.824
$a = b$	3.048	3.046	3.048	3.048
c	22.986	23.064	23.085	23.472

(Allmann 1970; Ookubo et al. 1993) and are not affected by the hydration time or the modification with *mbeeg*. On the other hand, the basal distance $d_{(003)}$ and consequently the lattice parameter c increase from HT–CO_3^{2-} to HT–OH^--16 h and with the hydration time from 16 to 21 h. However, the most pronounced increase is observed after the modification with *mbeeg*. For hydrotalcite-like compounds the basal distance d along the c-axis depends on the size and orientation of the anions and guest molecules in the gallery (Cavani et al. 1991). The thickness of the brucite layer is 4.8 Å (Cavani et al. 1991) and by subtracting it to the basal distance $d_{(003)}$ a gallery height of ca. 3 Å is obtained for HT–OH^-–*mbeeg*. This value is comparable to the size of the hydrophilic section of *mbeeg* molecule, the glycol ether function, along its y axis as it is shown in Scheme 1. This result, in combination to FT-IR and CHNS analysis, indicates that the hydrophilic section of *mbeeg* molecule was intercalated in the gallery, Scheme 1. Nevertheless, the increase of the inter-layer spacing could be an artifact since it was reported that if the morphology of the hydrotalcite-like compound is composed of very thin platelets it leads to the basal reflection being shifted to a slightly lower angle, giving an apparent spacing that is greater than the true value of c (Evans and Slade 2006).

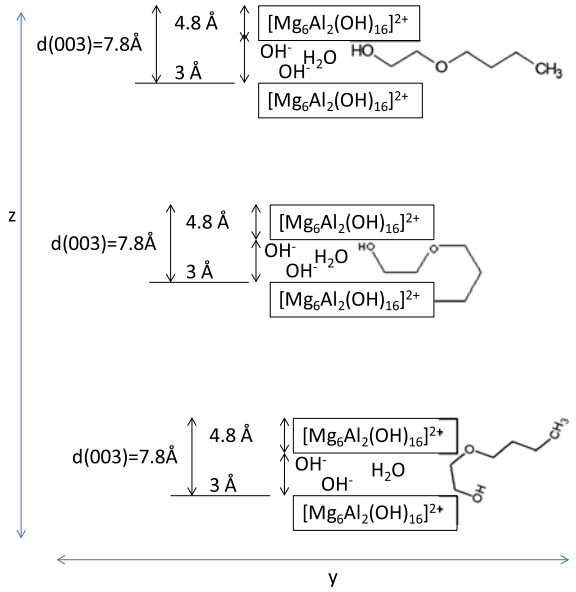

Scheme 1 Schematic representation of possible configurations adopted by monobutylether ethylene glycol interacting with the layered double hydroxide

TEM analysis

Transmission electron microscopy was performed to monitor changes in the morphological features of the synthesized samples. Representative TEM micrographs are depicted in Fig. 3. As it can be seen, the particle size, shape, and agglomeration change significantly between samples. HT–CO_3^{2-} and HT–OH^--16 h samples exhibit the hexagonal platelet morphology characteristic of hydrotalcite compounds, while in the case of HT–OH^--21 h and HT–OH^-–*mbeeg* their shape has become less well defined. The dimensions of HT–CO_3^{2-} platelets vary between 120 and 150 nm in plane and 50 nm in thickness. HT–OH^--16 h is formed of stacked hexagonal platelets, but of much lower dimensions forming large agglomerates of 1–1.5 μm, while HT–OH^--21 h is mainly formed by dispersed thin platelets of 20–25 nm. In the case though of HT–OH^-–*mbeeg*, the particles adopt a rough texture and they are formed of platelets with an ill-defined shape and aggregated in a face-to-face way. As mentioned above, *mbeeg* is a moderate surfactant. While its hydrophilic part interacts with the positively charged Mg–Al hydroxide layers, the affinity between the small aliphatic chains could be responsible for the aggregation of the HT–OH^-–*mbeeg* platelets.

N_2 and water sorption measurements

As suggested by Yun and Pinnavaia (1995) the face-to-face overlapping of crystallites generates interfaces that can accommodate extrinsic surface water, as well

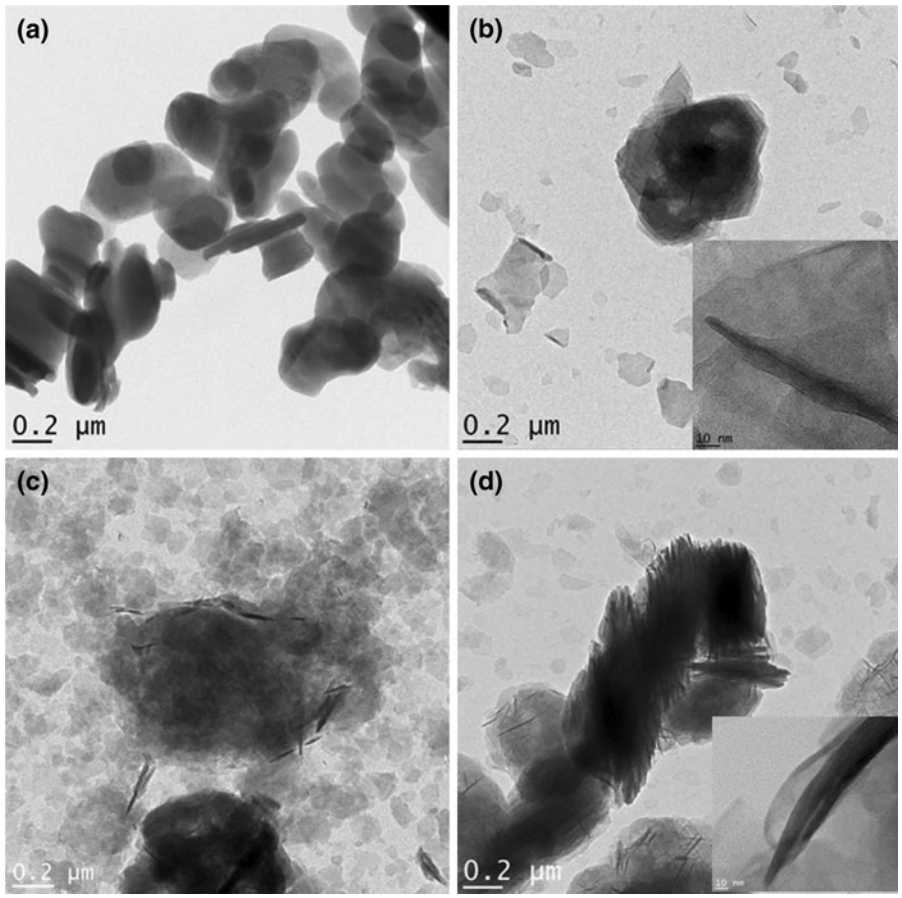

Fig. 3 TEM micrographs of HT–CO_3^{2-} (**a**), HT–OH^--16 h (**b**), HT–OH^--21 h (**c**), and HT–OH^-–*mbeeg* (**d**) samples. The *insets* of figures **b** and **d** have a *scale bar* 10 nm

as other adsorbates. Nitrogen and water sorption isotherms were recorded for all four samples so as to evaluate their textural properties and water sorption capacity.

As shown in Fig. 4a, the N_2 isotherms are of type IV according to IUPAC classification and are characteristic of mesoporous materials (Condon 2006) All isotherms present an H3 type hysteresis loop in the 0.45–0.95 partial pressure range, which is generally associated to aggregates with narrow slit pores of plate-like particles (Valente et al. 2009). In the case of HT–CO_3^{2-}, the hysteresis loop is very narrow, but it becomes more pronounced for HT–OH^- and HT–OH^-–*mbeeg*. The shape of the hysteresis loops can be interpreted in terms of the specific pore structure. In the case of HT–OH^-–*mbeeg*, the hysteresis loop tends to be almost vertical and parallel over a rather wide range of relative pressures. This type of hysteresis loop is observed in the case of aggregates of plate-like particles (Yun and Pinnavaia 1995). The above finding is supported by the TEM image of HT–OH^-–*mbeeg* that shows this type of microtexture.

The pore size distribution plots are reported in Fig. 4b, and the textural properties of the modified LDHs and pristine HT–CO_3^{2-} are summarized in Table 3. The HT–OH^-–*mbeeg* has a very high specific surface area (80 $m^2\ g^{-1}$) and higher total pore volume than all other LDHs. HT–CO_3^{2-} has broad unimodal pore size distribution in the mesopore range (20–60 Å), whereas the two HT–OH^- have a bimodal pore size distribution in the meso (20–60 Å) and the macropore range (100–1,000 Å); the macropore volume increases with the hydration time. HT–OH^-–*mbeeg* also shows a bimodal pore size distribution, but the modification with *mbeeg* clearly decreases the average pore diameters: the diameter of the smaller

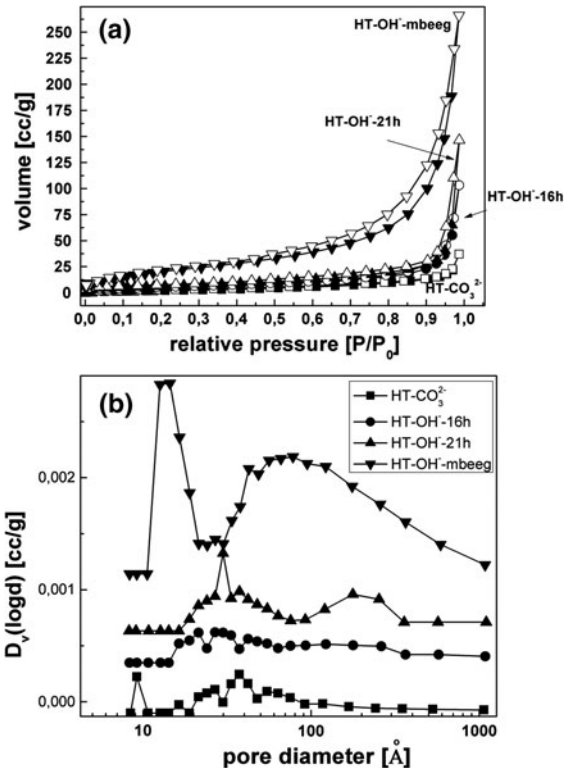

Fig. 4 **a** Nitrogen sorption isotherms for HT–CO_3^{2-} (*closed square*, *open square*), HT–OH^--16 h (*closed circle*, *open circle*), HT–OH^--21 h (*closed triangle*, *open triangle*) and HT–OH^-–*mbeeg* (*closed inverted triangle*, *open inverted triangle*) samples. The *close* and *open symbols* are for adsorption and desorption, respectively

pores is within 10–20 Å and is even lower than that of pristine HT–CO_3^{2-}. The average pore diameter values are reported in Table 3.

The changes detected after hydration and modification with *mbeeg* can be explained by the differences in the crystal size and stacking as seen by TEM. Upon hydration, the observed macroporosity is attributed to the aggregation of the particles toward larger agglomerates, increasing thus the inter-particle voids. Thus, the increase of the specific surface area of the DLH through the addition of a very small quantity of *mbeeg* can be ascribed mainly to an augmentation of the pore volume because of a more extended agglomeration. Though, *mbeeg* has a negative effect on the pore size diameters resulting in a 50 % decrease compared to the value obtained for HT–OH^--21 h.

The water sorption isotherms are presented in Fig. 5. Before recording the isotherms, the samples were pre-conditioned at 25 °C for 6 h under nitrogen flow. Under such conditions, the mass loss corresponds only to the loss of physisorbed and interparticle pore water and not to desorption of water in the gallery as temperature higher than 200 °C is required to eliminate this type of water (Yun and Pinnavaia 1995). During the sorption cycle, the mass increases steadily due to adsorption of water on the external surface of the LDHs. For HT–OH^- and HT–OH^-–*mbeeg*, a steeper increase of the water uptake is seen after 80 %RH due to the filling of interparticle pores. At high relative humidity, the water uptake increases considerably from HT–CO_3^{2-} to HT–OH^--16 h and HT–OH^--21 h samples, but it is even more pronounced for HT–OH^-–*mbeeg*, Table 3. Indeed, at 97 %, the water uptake for HT–CO_3^{2-} is less than 1 wt%, whereas for HT–OH^-–*mbeeg* it is 26.2 wt%. It can be concluded that the HT–OH^-–*mbeeg* has the highest water sorption capacity as the result of its elevated specific surface area. DVS results are consistent with TEM observations and the N_2 physisorption measurements. Indeed, similar to the N_2 physisorption measurements, the hysteresis loop in the water sorption isotherms increases as follows HT–CO_3^{2-} < HT–OH^--16 h ≈ HT–OH^--21 h < HT–OH^-–*mbeeg*. The hysteresis loop of HT–OH^-–*mbeeg*

Table 3 Specific surface area (*SSA*), total pore volume (V_T), average pore diameter (ϕ), water uptake (W_{up}), and proton conductivity (σ) for all samples

Parameter	HT–CO_3^{2-}	HT–OH^--16 h	HT–OH^--21 h	HT–OH^-–*mbeeg*
SSA ($m^2\ g^{-1}$)	8	17	22	79
V_T ($cm^3\ g^{-1}$)	0.057	0.16	0.23	0.41
ϕ (I) (nm)	37	32	40	14
ϕ (II) (nm)	–	298	392	79
W_{up} (21 °C, 98 % RH) (wt%)	0.84	18.33	19.25	26.24
σ (21 °C, 98 % RH) ($S\ cm^{-1}$)	1.07×10^{-5}	6.26×10^{-5}	1.61×10^{-3}	7.53×10^{-4}

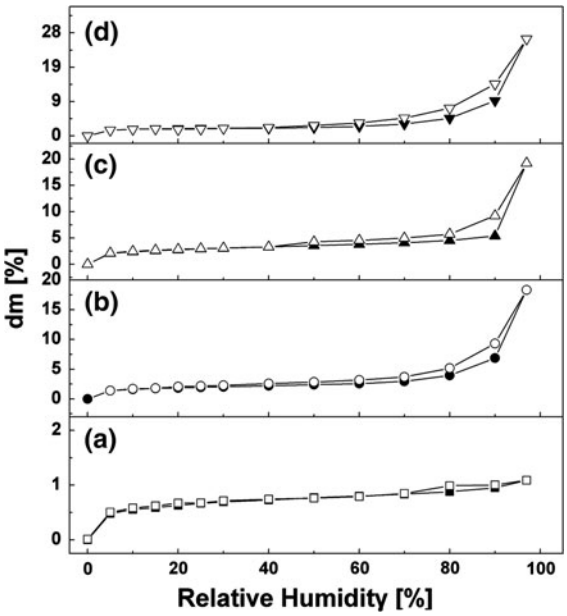

Fig. 5 Water sorption isotherms of HT–CO_3^{2-} (*closed square*, *open square*), HT–OH^--16 h (*closed circle*, *open circle*), HT–OH^--21 h (*closed triangle*, *open triangle*) and HT–OH^-–*mbeeg* (*closed inverted triangle*, *open inverted triangle*) samples recorded at 21 °C. The *close* and *open symbols* are for adsorption and desorption, respectively

extends to low relative pressures (RH = 30 %) as the result of the extended pore network.

AC impedance spectroscopy

The conductivity of the LDHs was measured by electrochemical impedance spectroscopy as a function of the temperature at RH = 98 %. As the three HT–OH samples differ in terms of specific surface area, particle size, and water sorption capacity, an attempt to analyze the conductivity data in terms of contribution from the intrinsic (*in the gallery*) conductivity and extrinsic (*inter-particle*) conductivity is done. It is important to mention that a detailed assessment of hydrotalcite-like compounds is missing (Tamaki et al. 2012). For this purpose, the comparison of impedance data of HT–OH materials with HT–CO_3^{2-} precursor is quite useful because of the different anion in the gallery.

Figures 6a, b show the Nyquist plots recorded for HT–CO_3^{2-} between 80 and 140 °C (heating cycle). The impedance spectra recorded up to 80 °C are characterized by a semicircle at high frequencies associated to the ion conduction and a low frequency ($f < \sim 10^2$ Hz) tail due to electrode blocking effect. These spectra are similar to those previously reported for these compounds (Furukawa et al. 2011; Kim et al. 2010). Interestingly, the semicircle splits into two semicircles in the 90–130 °C interval, but above 140 °C the two semicircles merge again into one component. Splitting of the semicircle reappears during impedance measurements taken upon cooling. The total resistance associated to both semicircles decreases with the temperature as expected for thermal activated processes. It has been reported previously that at high relative humidity and for temperatures higher than 70 °C, the hydrotalcite gallery expands to accommodate more water (Mokhtar et al. 2010). The combination of higher temperature with higher water content in the gallery is expected to substantially enhance the mobility of the gallery anion. Therefore, the semicircle at intermediate frequencies, which appears at a temperature slightly higher than 70 °C, can be ascribed to the motion of the carbonate ion in hydrotalcite gallery (intrinsic conductivity).

The intermediate frequency semicircle is absent in all spectra recorded for the three HT–OH samples, as illustrated in Fig. 7a for HT–OH^--16 h. Such feature adds further evidence that the intermediate frequency semicircle in Fig. 6 can be ascribed to the motion of carbonate anions in the gallery. But, to further understand the origin of the semicircle observed at high frequencies, the EIS spectra collected at room temperature for HT–OH^--16 h as a function of the equilibration time is shown in Fig. 7b. As the equilibration time increases, the sample absorbs more and more water and the resistance drops pronouncedly indicating that the magnitude of the conductivity is tuned by the amount of absorbed water. This relation between water content and the ion conductivity is often found in the study of layered and porous inorganic materials (Casciola et al. 1993; Colomer and Anderson 2001; Felice and Tavares 2011; Mikhailenko et al. 2002). It is worth to recall that the gallery of the LDH is saturated with water as a temperature higher than 200 °C is required to eliminate this type of water (Yun and Pinnavaia 1995). As shown above, by exposing the samples to high relative humidity, water not only adsorbs on the particles' external surface but also fills the inter-particles' pores. Consequently, water enables the ion transport through the porous network formed by the particles via the

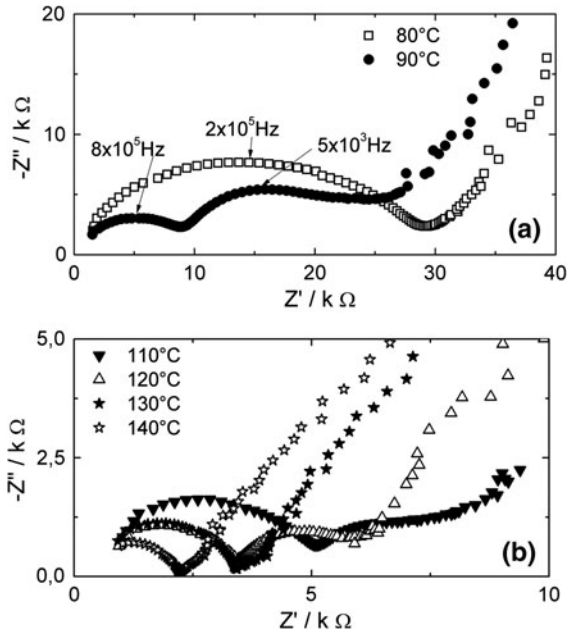

Fig. 6 Nyquist diagrams of HT–CO_3^{-2} at **a** 80 and 90 °C and **b** between 110 and 140 °C; **c** phase–frequency plot of HT–CO_3^{-2} between 80 and 150 °C

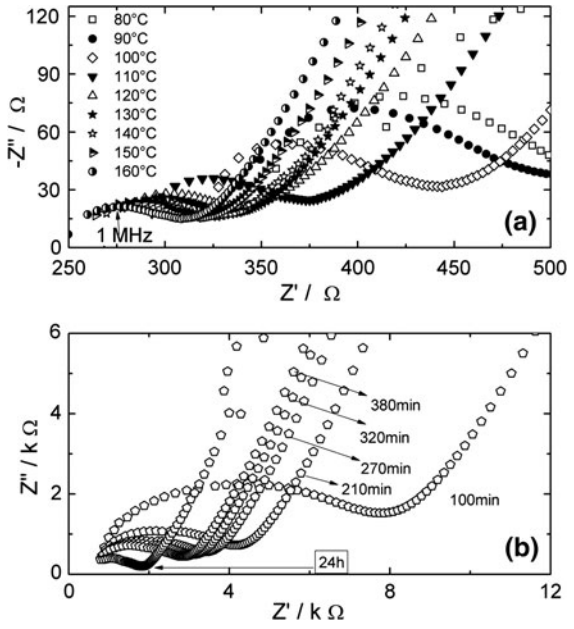

Fig. 7 Nyquist diagrams obtained for HT–OH^--16 h **a** as a function of time samples during the equilibration period in the conductivity cell at 30 °C and RH = 98 %; **b** between 80 and 250 °C

facile Grotthuss mechanism (Colomer and Anderson 2001, Mikhailenko et al. 2002). The strong dependence of the samples' resistance with the hydration time (or physisorbed and inter-particle water content) indicates that the high frequency semi-circle is related to the inter-particles' conductivity. However, since both the extrinsic and intrinsic hydroxide ion transport occur via Grotthuss mechanism, it is likely that ions in both regions of the material have similar relaxation frequencies, which results in a single convoluted semicircle at high frequency in the impedance diagrams.

Still, additional insights on the intrinsic versus inter-particle conductivity can be deduced from the temperature dependence of the total electrical conductivity extracted from the impedance diagrams. Figure 8 shows the Arrhenius plots for all four samples at RH = 98 %. As depicted in Fig. 8, the conductivity data taken upon heating and cooling do not overlap, and lower values were measured upon cooling. In addition, data taken upon heating show three distinct $\ln\sigma - 1/T$ dependences. On heating, HT–CO_3^{2-} presents two well-defined linear slopes, at low (20–60 °C; apparent activation energy $E_a = 0.19$ eV) and at high (120–180 °C; apparent $E_a = 0.31$ eV) temperature. At intermediate temperatures, where the two semicircles coexist in the Nyquist plot, the ion conductivity has a non linear dependence with $1/T$. On cooling from 180 to 60 °C, only one slope is found and the high value of activation energy (0.46 eV) is consistent with the conduction of carbonate anion in the gallery (De Roy and Besse 1991). The $\ln\sigma - 1/T$ behavior of the commercial HT–CO_3^{2-} differs from the one previously reported for Mg–Al–CO_3^{2-} by Kim et al. (2010) in which a high conductivity and low apparent activation energy was kept during the cooling cycle. Our data show that, in the present experimental conditions, the carbonate anions were not eliminated from the gallery during the heating cycle. Indeed, a temperature higher than 200 °C was reported to be necessary to achieve a high degree of conversion of HT–CO_3^{2-} to its OH^- form (Mokhtar et al. 2010).

For HT–OH^--16 h and HT–OH^--21 h, the apparent E_a values upon heating are within 0.14–0.18 eV for 20–60 °C interval, 0.21–0.25 eV for 60–90 °C, and 0.05–0.07 eV above 90 °C. A low value of activation energy ($E_a < 0.1$ eV) was previously reported and attributed to the ion hopping inside Mg–Al LDH galleries via Grotthuss mechanism (Kim et al. 2010). However, this value is lower than the typical ones reported for hydronium or hydroxide

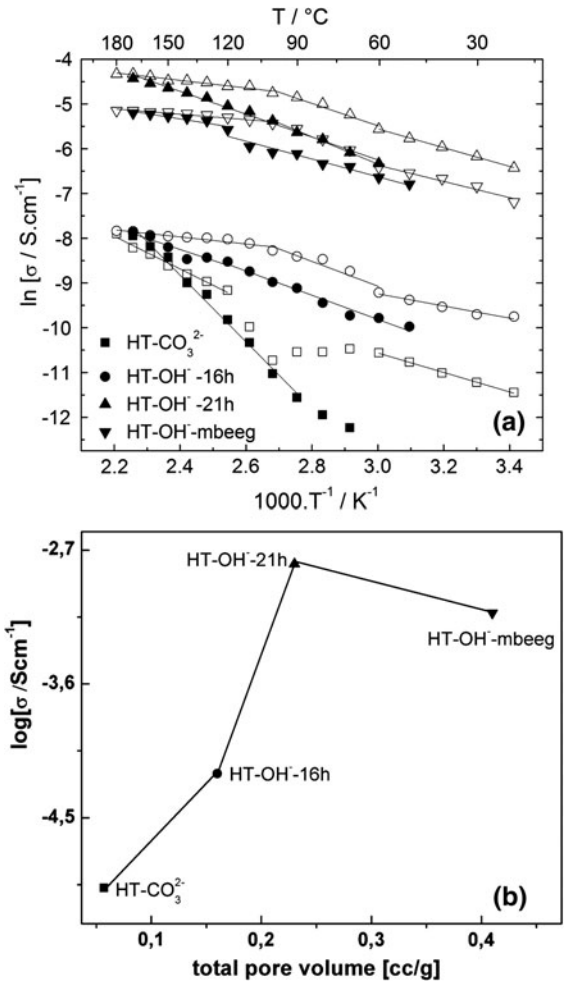

Fig. 8 **a** Arrhenius plot for the ion conductivity of HT–CO_3^{2-} (*closed square*, *open square*), HT–OH^--16 h (*closed circle*, *open circle*), HT–OH^--21 h (*closed triangle*, *open triangle*) and HT–OH^-–*mbeeg* (*closed inverted triangle*, *open inverted triangle*); **b** variation of the conductivity at 21 °C with the double layered hydroxides' total pore volume. The *open symbols* are for heating and the *close symbols* for cooling

conduction (~0.10 and 0.12 eV) (Agmon 2000). In contrast to HT–CO_3^{2-}, the weak temperature dependence of the conductivity above 90 °C suggests a limitation to ion transport in HT–OH^--16 h and HT–OH^--21 h samples. Deviations from the Arrhenius law were also reported for Zr-Cr-CO_3^{2-} LDHs (De Roy and Besse 1991) and due to the specific experimental conditions used in their work (imposed global hydration of each sample), this was explained in terms of evolution of the ratio between extrinsic and intrinsic water with temperature (De Roy and Besse 1991). On cooling down to 60 °C, HT–OH^--16 h and HT–OH^--21 h present only one slope and an activation energy of ~0.22 eV, which is consistent with hydroxide conduction inside the gallery (Furukawa et al. 2011). Indeed, the activation energy is slightly higher than the one reported for hydroxide ion conduction via Grotthuss mechanism (~0.12 eV) (Agmon 2000), indicating that the lower mobility of coordinated water molecules inside the hydrotalcite inter-layers slows down the ion conduction.

The difference between the E_a values for HT–CO_3^{2-}, HT–OH^--16 h, and HT–OH^--21 h on heating and cooling cycles can probably be accounted for the water sorption/desorption behavior typical of such compounds (Hou et al. 2003), Fig. 5. The conductivity measurements on heating above ~100 °C are probably accompanied by the inter-layer gallery expansion as a result of the extrinsic to intrinsic water conversion. Most likely, during the heating cycle the LDH structure is not in equilibrium with the surrounding humidified environment. However, owing to its capacity to retain intrinsic water, the samples attained a relatively stable structure during the cooling cycle and the typical values activation energies for the CO_3^{2-} and OH^- ions in the gallery (intrinsic conductivity) were obtained.

The apparent activation energy for HT–OH^-–*mbeeg* samples upon heating is within 0.16 eV for 20–60 °C interval, 0.26 eV for 60–90 °C, and 0.05 eV above 90 °C. The E_a values on cooling (0.17 eV from 120 to 50 °C and 0.10 eV from 180 to 120 °C) are close to those expected for the hydroxide anion conduction by Grothuss mechanism in liquid phase, suggesting that the inter-particle conduction is the preponderant mechanism in this case. Indeed, this LDH has the highest water uptake and shows the lowest hysteresis between the heating and cooling cycles.

Thus, it can be concluded that under the present experimental conditions, both intrinsic and inter-particle processes contribute to the total conductivity of HT–CO_3^{2-}, HT–OH^--16 h, and HT–OH^--21 h measured during the heating cycle and up to ca. 80 °C. During the cooling cycle, the intrinsic conduction is the preponderant pathway for these three materials and the total conductivity is lower than the one recorded during the heating cycle. For HT–OH^-*mbeeg*, the inter-particle conductivity seems to be preponderant for ion conduction on both heating and cooling cycles.

Overall, the total conductivity increases as follows: HT–CO_3^{2-} < HT–OH^--16 h < HT–OH^-–*mbeeg* < HT–OH^--21 h. At room temperature, the ion conductivity of HT–OH^-–*mbeeg* and HT–OH^--21 h is two orders of magnitude higher than hydrotalcite and one order of magnitude higher than HT–OH^--16 h, Table 3. However, at room temperature the conductivity of HT–OH^--21 h (1.61×10^{-3} S cm^{-1}) is lower than the one reported for $Mg_{1-x}Al_x$–OH type with $x = 0.25$ ($\sim 4 \times 10^{-3}$ S cm^{-1}) (Kim et al. 2010) and differences in the particle size could explain such variation (Tamaki et al. 2012). The trend found for the ion conductivity and the lower value measured for HT–OH^-–*mbeeg* versus HT–OH^--21 h suggests a trade-off between the (increasing) water sorption capacity of the samples and their textural properties (average pore size vs specific surface area), Fig. 8b. Larger amount of intercalated water facilitates the ion conductivity in the gallery and the extrinsic adsorbed water available favors the inter-particle (extrinsic) ion conduction (Lal and Howe 1981). On the other hand, a high specific surface area and low average pore volume as in HT–OH^-–*mbeeg* suggest a longer and tortuous diffusion path for ion hopping, and therefore lower inter-particle ion conductivity.

Though the modification of HT–OH^- compounds with *mbeeg* was successful in terms of water uptake and retention of water, its effect on the textural and conduction properties was negative: the overall balance is lower ion conductivity for the *mbeeg* modified compound with respect to HT–OH^--21 h. Further investigations are in progress. In particular, we focus on measuring the conductivity at lower relative humidity, on the effect of *mbeeg* content on the textural and conductivity properties of the HT–OH^- compounds, as well as on the study of the water diffusion by dynamic vapor sorption.

Conclusions

Mg–Al layered double hydroxides with OH^- anions in the gallery were prepared from commercial HT–CO_3^{2-} by the reconstruction method and further modified with *mbeeg* a mild surfactant. TEM analysis showed that the two HT–OH^- and HT–OH^-–*mbeeg* are formed by nanoplatelets of lateral dimension inferior to 20 nm, but *mbeeg* induces the formation of micrometer size agglomerates of nanoplatelets in a face-to-face configuration. This unique morphology results in a LDH material with very high specific surface area (80 m^2 g^{-1} vs 20 m^2 g^{-1} for HT–OH^- samples prepared without *mbeeg*) attributed to the formation of an extended network of relatively narrow inter-particle pores. The *mbeeg*-modified LDH has higher water sorption capacity than HT–OH^--21 h (26.24 vs 19.25 wt% at 21 °C and 97 %RH), but a lower ion conductivity (7.53×10^{-4} vs 1.61×10^{-3} S cm^{-1} at 21 °C and 98 %RH). The lower ion conductivity and lower average pore diameters found for HT–OH^-–*mbeeg* suggest the existence of dead ends and/or tortuosity on the extended network of inter-particle pores that hinder the ion transport; under such conditions, not all adsorbed surface water is effective for ion transport. The activation energy values determined from the cooling cycle are consistent with the nature of the anion in the gallery (CO_3^{2-} or OH^-) for HT–CO_3^{2-}, HT–OH^--16 h, and HT–OH^--21 h. For HT–OH^-–*mbeeg*, low apparent activation energy values (0.10 eV from 180 to 120 °C and 0.17 eV from 120 to 50 °C) were found suggesting that the inter-particle mechanism is preponderant. Further studies on DLH samples with different *mbeeg* content are being carried out to correlate the conducting mechanism with the structural and textural properties of these materials, and to get more insights on the dependence of the electrical conductivity with temperature and relative humidity.

Acknowledgments This work was realized with the financial support of the FRQNT (Quebec), MDEIE (Quebec), the Canadian Foundation for Innovation, CAPES (Brazil) and CNPq (Brazil). M. J. Paulo thanks INRS-EMT for exemption of supplemental tuition fees.

References

Agmon N (2000) Mechanism of hydroxide mobility. Chem Phys Lett 319:247–252. doi:10.1016/S0009-2614(00)00136-6

Alberti G, Casciola M, Massinelli L, Bauer B (2001) Polymeric proton conducting membranes for medium temperature fuel cells (110–160°C). J Membr Sci 185:73–81. doi:10.1016/S0376-7388(00)00635-9

Allmann R (1968) The crystal structure of pyroaurite. Acta Crystallogr B24:972–977. doi:10.1107/S0567740868003511

Allmann R (1970) Double layer structures with brucite-like ions $[M(II)_{1-x}M(III)_x(OH)^{2x+}]$. Chimia 24:99–108

Aramendia MA, Avilés Y, Benitez JA, Borau V, Jiménez C, Marinas JM, Ruiz JR, Urbano FJ (1999) Comparative study of Mg/Al and Mg/Ga layered double hydroxides.

Microporous Mesoporous Mater 29:319–328. doi:10.1016/S1387-1811(98)00345-X

Béres A, Pálinkó I, Kiricsi I, Nagy JB, Kiyozumi Y, Mizukami F (1999) Layered double hydroxides and their pillared derivatives–materials for solid base catalysis; synthesis and characterization. Appl Catal A 182:237–247. doi:10.1016/S0926-860X(99)00009-5

Borgohain MM, Joykumar T, Bhat SV (2010) Studies on nanocomposite solid polymer electrolyte with hydrotalcite as a filler. Solid State Ion 181:964–970. doi:10.1016/j.ssi.2010.05.040

Bröcker FJ, Kainer L (1970) German Patent 2,024,282 to BASF AG

Casciola M, Marmottini F, Peraio A (1993) AC conductivity of a-layered zirconium phosphate in the presence of water vapour at 100–200°C. Solid State Ionics 61:125–129. doi:10.1016/0167-2738(93)90344-3

Cavani F, Trifiro F, Vaccari A (1991) Hydrotalcite-type anionic clays: preparation, properties and applications. Catal Today 11:173–301. doi:10.1016/0920-5861(91)80068-K

Cho MS, Shin B, Choi SD, Lee Y, Song KG (2004) Gel polymer electrolyte nanocomposites PEGDA with Mg–Al layered double hydroxides. Electrochim Acta 50:331–334. doi:10.1016/j.electacta.2004.03.050

Colomer MT, Anderson MA (2001) High porosity silica xerogels prepared by a particulate sol–gel route: pore structure and proton conductivity. J Non Cryst Solids 290:93–104. doi:10.1016/S0022-3093(01)00815-8

Condon JB (2006) Surface area and porosity determinations by physisorption, measurements and theory. Elsevier, The Netherlands

Crupi MP, Jannelli S, Magazu G, Maisano D, Majolino P, Migliardo D, Sirna D (1995) Rayleigh wing and Fourier transform infrared studies of intermolecular and intramolecular hydrogen bonds in liquid ethylene glycol. Mol Phys 84:645–652. doi:10.1080/00268979500100431

Crupi MP, Jannelli S, Magazu G, Maisano D, Majolino P, Migliardo P, Ponterio R (1996) Raman spectroscopic study of water in the poly(ethylene glycol) hydration shell. J Mol Struct 381:207–212. doi:10.1016/0022-2860(96)09308-8

De Roy A, Besse JP (1989) Conductivité ionique de composées de type hydrotalcite. Solid State Ion 35:35–43. doi:10.1016/0167-2738(89)90009-X

De Roy A, Besse JP (1991) Evolution of protonic conduction in some synthetic anionic clays. Solid State Ion 46:95–101. doi:10.1016/0167-2738(91)90135-X

De Roy A, Besse JP, Bondot P (1985) Structural approach and conductivity of lamellar hydroxides $Zn_2Cr(OH)_6X{\cdot}nH_2O$ (x = anion) by xanes, exafs and X-ray diffraction. Mater Res Bull 20:1091–1098. doi:10.1016/0025-5408(85)90209-0

Evans DG, Slade RCT (2006) Structural aspects of layered double hydroxides. Struct Bond 119:1–87. doi:10.1007/430_005

Felice V, Tavares AC (2011) Faujasite zeolites as solid electrolyte for low temperature fuel cells. Solid State Ion 194:53–61. doi:10.1016/j.ssi.2011.05.006

Feng YJ, Li DQ, Li CX, Wang ZH, Evans DG, Duan X (2003) Synthesis of Cu-containing layered double hydroxides with a narrow crystallite-size distribution. Clays Clay Miner 51:566–569. doi:10.1346/CCMN.2003.0510510

Furukawa Y, Tadanaga K, Hayashi A, Tatsumisago M (2011) Evaluation of ionic conductivity for Mg–Al layered double hydroxide intercalated with inorganic anions. Solid State Ion 192:185–187. doi:10.1016/j.ssi.2010.05.032

Gusmano G, Nunziante P, Traversa E, Chiozzini G (1991) Study of the thermal behaviour of hydroxide mixtures aimed at the preparation of Mg–Al spinels. J Therm Anal Calorim 37:1697–1707. doi:10.1007/BF01912199

Hickner MA (2010) Ion-containing polymers: functional materials for new energy and clean water. Mater Today 13:34–41. doi:10.1016/S1369-7021(10)70082-1

Hou X, Bish DL, Wang SL, Johnston CT, Kirkpatrick RJ (2003) Hydration, expansion, structure, and dynamics of layered double hydroxides. Am Miner 88:167–169

Hussein MZ, Hwa TK (2000) Synthesis and properties of layered organic–inorganic hybrid material: Zn–Al layered double hydroxide–dioctyl sulfosuccinate nanocomposite. J Nanopart Res 2:293–298. doi:10.1023/A:1010013201391

Kim HS, Yamazaki Y, Kim JD, Kudo T, Honma I (2010) High ionic conductivity of Mg–Al layered double hydroxides at intermediate temperature (100–200°C) under saturated humidity condition (100% RH). Solid State Ion 181:883–888. doi:10.1016/j.ssi.2010.04.037

Lal M, Howe AT (1980) High proton conductivity in pressed pellets of zinc–chromium hydroxide. J Chem Soc Chem Commun 1980:737–738. doi:10.1039/C39800000737

Lal M, Howe AT (1981) Studies of zinc–chromium hydroxy salts. II. Composite anion conductors of pressed disks of $[Zn_2Cr(OH)_6]X{\cdot}nH_2O$, where X^-=F^-, Cl^-, Br^-, I^-, NO_3^-, and CO_3^{2-}. J Solid State Chem 39:377–386. doi:10.1016/0022-4596(81)90273-5

Lee K, Nam JD (2006) Optimum ionic conductivity and diffusion coefficient of ion-exchange membranes at high methanol feed concentrations in a direct methanol fuel cell. J Power Sources 157:201–206. doi:10.1016/j.jpowsour.2005.07.059

Lee K, Nam JH, Lee JH, Lee Y, Cho SM, Jung CH, Choi HG, Chang YY, Kwon YU, Nam JD (2005) Methanol and proton transport control by using layered double hydroxide nanoplatelets for direct methanol fuel cell. Electrochem Commun 7:113–118. doi:10.1016/j.elecom.2004.11.011

Li XD, Yang WS, Li F, Evans DG, Duan X (2006) Stoichiometric synthesis of pure $NiFe_2O_4$ spinel from layered double hydroxide precursors for use as the anode material in lithium-ion batteries. J Phys Chem Solids 67:1286–1290. doi:10.1016/j.jpcs.2006.01.096

Liao CS, Ye WB (2003) Enhanced ionic conductivity in poly(ethylene oxide)/layered double hydroxide nanocomposite electrolytes. J Polym Res 10:241–246. doi:10.1023/b:jpol.0000004619.00197.7a

Mikhailenko S, Desplantier-Giscard D, Danumah C, Kaliaguine S (2002) Solid electrolyte properties of sulfonic acid functionalized mesostructured porous silica. Microporous Mesoporous Mater 52:29–37. doi:10.1016/S1387-1811(02)00275-5

Miyata S (1975) The syntheses of hydrotalcite-like compounds and their structures and physico-chemical properties. Clays Clay Miner 23:369–375. doi:10.1346/CCMN.1975.0230508

Miyata S (1983) Anion-exchange properties of hydrotalcite-like compounds. Clays Clay Miner 31:305–311. doi:10.1346/CCMN.1983.0310409

Miyata S, Okada A (1977) Synthesis of hydrotalcite-like compounds and their physicochemical properties—the systems

Mg^{2+}–Al^{3+}–SO_4^{2-} and Mg^{2+}–Al^{3+}–CrO_4^{2-}. Clays Clay Miner 25:14–18. doi:10.1346/CCMN.1977.0250103

Miyazaki K, Abe T, Nishio K, Nakanishi H, Ogumi Z (2010) Use of layered double hydroxides to improve the triple phase boundary in anion-exchange membrane fuel cells. J Power Sources 195:6500–6503. doi:10.1016/j.jpowsour.2010.04.023

Mokhtar M, Inayat A, Ofili J, Schwieger W (2010) Thermal decomposition, gas phase hydration and liquid phase reconstruction in the system Mg/Al hydrotalcite/mixed oxide: a comparative study. Appl Clay Sci 50:176–181. doi:10.1016/j.clay.2010.07.019

Moneyron JE, De Roy A, Besse JP (1991) Protonic conductivity of hydrotalcite-type compound thick films: application to a humidity sensor. Solid State Ion 46:175–181. doi:10.1016/0167-2738(91)90147-4

Muksing N, Magaraphan R, Coiai S, Passaglia E (2011) Effect of surfactant alkyl chain length on the dispersion, and thermal and dynamic mechanical properties of LDPE/organo-LDH composites. Express Polym Lett 5:428–448. doi:10.3144/expresspolymlett.2011.42

Nguyen TT, Raupach M, Janik LJ (1987) Fourier-transform infrared study of ethylene glycol monoethyl ether adsorbed on montmorillonite; implications for surface area measurements of clays. Clays Clay Miner 35:60–67. doi:10.1346/CCMN.1987.0350108

Olfs HW, Torres-Dorante LO, Eckelt R, Kosslick H (2009) Comparison of different synthesis routes for Mg–Al layered double hydroxides (LDH): characterization of the structural phases and anion exchange properties. Appl Clay Sci 43:459–464. doi:10.1016/j.clay.2008.10.009

Ookubo A, Ooi K, Hayashi H (1993) Preparation and phosphate ion-exchange properties of a hydrotalcite-like compound. Langmuir 9:1418–1422. doi:10.1021/la00029a042

Paulo MJ, Tavares AC (2011) Novel hydrotalcite composites membranes for alkaline fuel cells. ECS Trans 35(31):21. doi:10.1149/1.3647850

Pernice P, Marino O, Masoolo G (1988) Influence of temperature and humidity on ionic conduction of mixed metal hydroxides. Thermochim Acta 13:87–92. doi:10.1016/0040-6031(88)87141-7

Philippova OE, Kuchanov SI, Topchieva IN, Kabanov VA (1985) Hydrogen bonds in dilute solutions of poly(ethylene glycol). Macromolecules 18:1628–1633. doi:10.1021/ma00150a018

Reeves V (2001) Layered double hydroxides: present and future. Nova Science, New York, p 140

Reichle WT (1986) Synthesis of anionic clay minerals (mixed metal hydroxides, hydrotalcite). Solid State Ion 22:135–141. doi:10.1016/0167-2738(86)90067-6

Rozenberg M, Loewenschuss A, Marcus Y (1998) IR spectra and hydration of short-chain polyethyleneglycol. Spectrochim Acta A 54:1819–1826. doi:10.1016/S1386-1425(98)00062-6

Stygar J, Zukowska G, Wieczorek W (2005) Study of association in alkali metal perchlorate–poly(ethylene glycol) monomethyl ether solutions by FT-IR spectroscopy and conductivity measurements. Solid State Ion 176:2645–2652. doi:10.1016/j.ssi.2005.07.006

Tadanaga K, Furukawa Y, Hayashi A, Tatsumisago M (2010) Direct ethanol fuel cell using hydrotalcite clay as a hydroxide ion conductive electrolyte. Adv Mater 22:4401–4404. doi:10.1002/adma.201001766

Tamaki T, Nakanishi N, Ohashi H, Yamaguchi T (2012) The effect of particle size and surface area on the ion conductivity of layered double hydroxide. Electrochem Comm 25:50–53. doi:10.1016/j.elecom.2012.09.003

Tichit D, Lhouty MH, Guida A, Chiche BH, Figueras F, Auroux A, Bartalini D, Garrone E (1995) Textural properties and catalytic activity of hydrotalcites. J Catal 151:50–59. doi:10.1006/jcat.1995.1007

Traversa E, Nunziante P, Chiozzini P (1992a) Thermal decomposition of Mg–Al hydroxides coprecipitated in the presence of oxalate ions. Thermochim Acta 199:25–33. doi:10.1016/0040-6031(92)80247-T

Traversa E, Montesperelli G, Nunziante P, Chiozzini G (1992b) The thermal behaviour of the hydroxide mixtures used for the synthesis of $MgFe_2O_4$ spinel. J Therm Anal Calorim 38:2583–2592. doi:10.1007/BF01979734

Trikeriotis M, Ghanotakis DF (2007) Intercalation of hydrophilic and hydrophobic antibiotics in layered double hydroxides. Int J Pharm 332:176–184. doi:10.1016/j.ijpharm.2006.09.031

Valente JS, Sanchez-Cantu M, Lima E, Figueras F (2009) Method for large-scale production of multimetallic layered double hydroxides: formation mechanism discernment. Chem Mater 21:5809–5818. doi:10.1021/cm902377p

Varcoe JR, Slade RC (2005) Prospects for alkaline anion-exchange membranes in low temperature fuel cells. Fuel Cells 5:187–200. doi:10.1002/fuce.200400045

Yang W, Kim Y, Liu PKT, Sahimi M, Tsotsis TT (2002) A study by in situ techniques of the thermal evolution of the structure of a Mg–Al–CO_3 layered double hydroxide. Chem Eng Sci 57:2945–2953. doi:10.1016/S0009-2509(02)00185-9

Yun SK, Pinnavaia TJ (1995) Water content and particle texture of synthetic hydrotalcite-like layered double hydroxides. Chem Mater 7:348–354. doi:10.1021/cm00050a017